Contributions to the Interfacial Adhesion in Co-Sintered Bilayers

Y. BOONYONGMANEERAT and C.A. SCHUH

The adhesive strength of co-sintered bilayers is influenced by several factors, including the nature of bonding along the joined interface, residual stresses evolved during processing, and the sintered properties of the individual layers. Here these separate contributions are isolated through careful control of the co-sintering process for W/Al_2O_3 bilayers, and in particular through control of the W-layer properties by using the process of activated sintering. Four-point bending delamination tests are used to evaluate adhesion and strength of the bilayers, and the interfacial fracture mechanics of the system is numerically studied using finite element simulations. Improvements in sintered density are found to increase the adhesive strength of the system only up to a point, beyond which shrinkage mismatch compromises the intrinsic toughness of the interface.

I. INTRODUCTION

BILAYERED composite materials can be found in many applications, ranging from the thin film-substrate systems used widely in the microelectronics industry to coating systems in structural applications.[1,2,3] Among the various processing techniques used to fabricate layered composites, co-sintering of layered materials, which involves simultaneous joining and consolidation of powders, is relatively common.[4,5,6] The advantages of co-sintering include its amenability to slurry-based processing routes, potential net-shape processing of complex geometries, and the incorporation of refractory materials at relatively low processing temperatures. While the performance-critical physical properties of co-sintered systems vary from one application to another, the adhesion between bonded layers is important for most layered composite systems, as it underpins the structural integrity of components.

The main factors controlling adhesion of co-sintered materials include (1) the nature of bonding along the joined interfaces, (2) residual stresses arising in the firing cycle, and (3) the degree of sintering and associated density-related mechanical properties of the individual layers of the composite. For co-sintering of nonreactive species, mechanical interlocking of sintered particles is often the key mechanism controlling point (1), while shrinkage mismatch (during sintering) and thermal expansion mismatch (during cooling) influence point (2). It is also clear that there may be significant interrelations between these issues and point (3); whereas longer sintering times may lead to stronger layers and stronger mechanical interlocking at the interface, it may also influence the development of shrinkage mismatch of the components, which can result in the formation of interfacial microcracks that compromise the strength of the joint.[7] Despite this synergy, points (1), (2), and (3) are usually treated separately in the literature. References 8–12, for example, are studies related to joining techniques for co-fired W/Al_2O_3, focusing on the nature of bonding without significant attention to residual stresses. References 13–17, on the other hand, involve studies of shrinkage and thermal mismatch induced in co-sintered materials but do not concern themselves with the density-related property changes of the individual sintered layers.

It is the purpose of this work to explicitly study the effects of the above points simultaneously, and to gain some understanding of their interaction as it affects the toughness of joints between co-sintered layers. In particular, the influences of the sintering variables and residual stresses on interfacial interlocking and the adhesion of co-sintered bilayer materials are investigated experimentally in the tungsten-alumina (W/Al_2O_3) system, and finite element simulations are employed to numerically study the interfacial fracture mechanics of the system.

II. EXPERIMENTAL

A. *Methods*

1. *Material system*

The material system chosen for the present work was W/Al_2O_3, which was selected for several important reasons. First, W/Al_2O_3 is a metal-ceramic system used to a great extent, especially for electronic packages and metal brazing applications;[18,19] a typical processing route to join the two materials involves slip-casting W-containing slurries onto Al_2O_3 substrates, followed by co-firing above 1500 °C. Second, it has been found that no primary chemical interaction occurs along the W/Al_2O_3 interface, and mechanical interlocking is the main mechanism that controls adhesion, even after firing at very high temperatures close to 2000 °C.[12,20,21] Third, the sintering kinetics of W particles can be dramatically changed by the addition of very small quantities of transition metals, such as Ni, Fe, and Pd, through the process of activated sintering,[22,23] and here we use this feature of the system to control the sintered strength and stiffness of the W layer as well as the shrinkage mismatch of co-sintered W/Al_2O_3.

A single lot of Al_2O_3 powder from Remet Corp. (Utica, NY) with a mean particle size of 4 μm (equivalent diameter) was used to prepare all specimens in this work. The W powders, on the other hand, were received from various suppliers and will be labeled with the letters A through C. Figure 1 presents the particle size distributions of the W

Y. BOONYONGMANEERAT, Graduate Research Assistant, and C.A. SCHUH, Salapatas Associate Professor of Metallurgy, are with the Department of Materials Science and Engineering, Massachusetts Institute of Technology, Cambridge, MA 02139. Contact e-mail: schuh@mit.edu

Manuscript submitted October 27, 2005.

powders, which were measured on a population basis using a scanning electron microscope to examine at least 300 randomly selected particles. The mean particle size and the content of Ni and Fe of each powder are shown in Table I; they differ due to the origin of the powders as well as the procedures we used.

Powder A was supplied by Alfa Aesar (Wardhill, MA) and had a relatively low impurity content. To manipulate the sintered density of this powder, various minority additions of Ni powder (2.2 to 3 μm) were added to the W powder by dry mixing following the procedure of Reference 24; these powders will be labeled with an additional number (*e.g.,* A-1, A-2) to differentiate between different Ni additions (Table I).

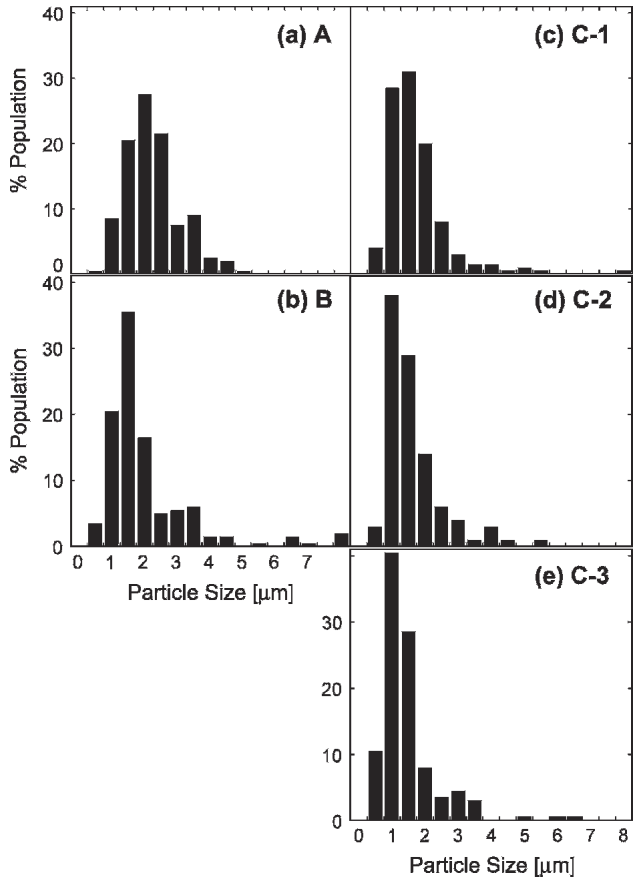

Fig. 1—Particle size distribution of the various W powders used in the study. Series A and B powders were all drawn from the same lot with the distributions shown in (*a*) and (*b*), while the series C powders were each from separate lots and had slight variations from one another, as shown for C-1 (*c*), C-2 (*d*), and C-3 (*e*).

Powder B was produced by Alldyne Powder Technologies (Huntsville, AL). This powder differed from powder A primarily in its relatively high initial content of sintering activators (Ni and Fe) present as impurities. The mean particle sizes of powder A and B were comparable (Table I), although the two powders had distinct particle size distributions (Figures 1(a) and (b)), with powder B having a more significant population of particles with particle size between 1 and 2 μm. Similar to the procedure used with powder A, powder B was mixed with various additions of Ni, and the resulting mixtures will be labeled B-2 to B-4 (Table I).

Powders C-1, C-2, and C-3, also produced by Alldyne Powder Technologies (Huntsville, AL), were chosen to more closely represent the kind of variability in powder character that might arise in an industrial setting. For example, impurities of both Ni and Fe were present as tramp elements in these powders and were somewhat different in samples C-1, C-2, and C-3. No additional Ni was mixed into the powders of this series, and the mean particle sizes and particle size distributions of the powders were all reasonably comparable to one another (Figures 1(c), (d), and (e)).

We report the concentration of sintering activators in terms of the average monolayer coverage of the additives, relative to the amount of W surface area in the system ($\bar{M}$) as shown in Table I. The average monolayer coverage was calculated by integrating monolayer coverage over the particle size distributions, assuming spherical particles:

$$\bar{M} = \frac{\int P(r) \frac{\left[r^3 + \frac{3c}{4\pi\rho}\right]^{\frac{1}{3}} - r}{2a} dr}{\int P(r)\, dr} \quad [1]$$

where r is the particle radius of W, P(r) is the number population of W powders at any particle size, and c, a, and ρ are the concentration, atomic radius, and theoretical density of the sintering activators, respectively.

Table I. Particle Size and Sintering Activator Contents of the Various W Powders Used in This Study

		Ni Content		Fe Content	
Powder	Mean Size (μm)	Wt Pct	# Monolayers	Wt Pct	# Monolayers
A-1	2.2	0.005	0.13	0	0
A-2	2.2	0.02	0.5	0	0
A-3	2.2	0.06	1.5	0	0
A-4	2.2	0.09	2.5	0	0
A-5	2.2	0.19	5.0	0	0
B-1	2.1	0.014	0.32	0.038	0.91
B-2	2.1	0.04	0.9	0.038	0.91
B-3	2.1	0.07	1.6	0.038	0.91
B-4	2.1	0.10	2.3	0.038	0.91
C-1	1.7	0.006	0.11	0.018	0.37
C-2	1.5	0.015	0.28	0.039	0.79
C-3	1.4	0.025	0.44	0.092	1.75

2. *Processing*

A two-layer compact joining specimen was the test geometry chosen for this work, for reasons that will become clear in the next section. To prepare such specimens, Al_2O_3 and W powder were sequentially loaded into a die of rectangular cross-section and cold pressed without binders using a single-action press at 80 MPa. These green specimens were then co-fired in a furnace programmed with a heating rate of 5 °C/min and an isothermal hold at 1177 °C for 1 hour, followed by slow furnace cooling. This cycle allows only modest sintering for both W and Al_2O_3, so the specimens tested in this work experienced only "initial stage" sintering and had relative densities below about 0.75 after processing. To prevent the oxidation of W, the processing was carried out in a dry 3 pct H_2/97 pct N_2 atmosphere. The geometry of each fired specimen was approximately 8.3 × 24.7 × 5.1 mm, with individual layer thicknesses for W and Al_2O_3 being 4.4 mm and 0.7 mm, respectively. These specimens differed from one another only in the character of the W powders, according to Table I.

Some typical test specimens are shown in Figure 2(a). In Figure 2(b), a magnified view of the interfacial region between W and Al_2O_3 is shown in a scanning electron micrograph. The interfacial character is similar to that seen in prior work on co-sintered W/Al_2O_3[12] and contains no obvious excess porosity as compared with that in the individual layers themselves. As expected, there is no sign of chemical reaction between the layers.

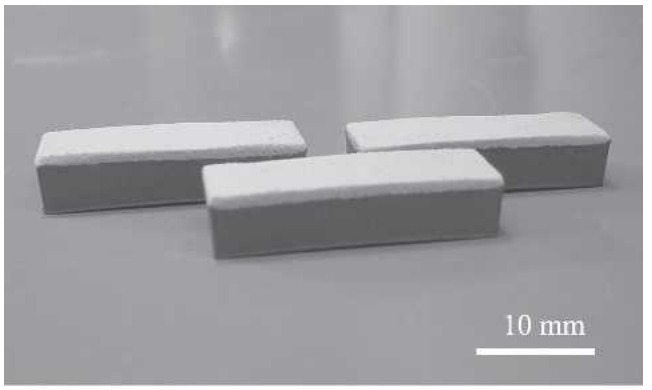

(*a*)

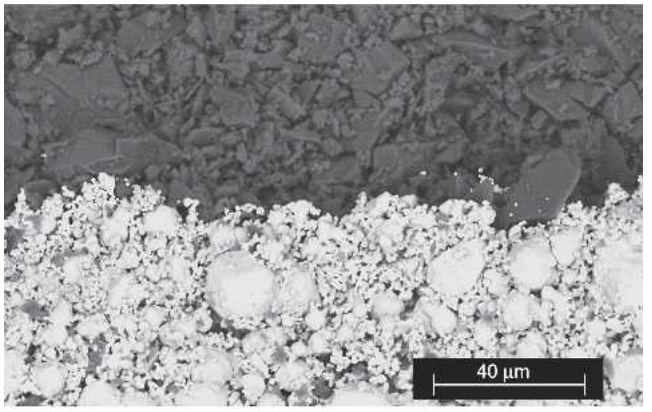

(*b*)

Fig. 2—Samples of bilayer specimens, prepared by cold pressing and firing at 1177 °C for 1 hour in a 3 pct H_2/97 pct N_2 atmosphere in (*a*) a macroscopic view and (*b*) a magnified view of the interfacial region, observed by scanning electron microscopy. In both views the layer on the bottom is composed of C-2 W powders and the layer on the top is Al_2O_3. The contrast in the images is opposite due to the two different modes of imaging.

3. *Mechanical testing*

To establish a baseline for understanding the properties of W/Al_2O_3 bilayers, mechanical tests were first performed on some free-standing W or Al_2O_3 specimens, produced using the same general procedures described above. Flexural elastic modulus of W and Al_2O_3 was assessed using standard three-point bending tests according to ASTM D790-03.

The adhesion of W/Al_2O_3 co-sintered specimens was evaluated using a four-point bending delamination test[25] with the geometry shown in the inset to Figure 3. This test has been used in a number of investigations to determine the bonding properties of interfaces[26–29] and was selected here because it allowed us to evaluate the interfacial fracture energy.[30] The tests were performed using a universal testing machine with a crosshead speed of 50 μm/min. Prior to the test, each specimen was prenotched in the middle of the sample (on the plane of symmetry) in the porous Al_2O_3 layer, using a razor blade.

B. *Experimental Results and Discussion*

Table II presents the measured linear sintering shrinkage and Young's modulus of free-standing Al_2O_3 and W specimens made with series C powders. The results clearly show that the degree of sintering, quantified here by the sintering shrinkage, improved with the increase of sintering activator concentration in the W powders. Elastic modulus is well known to increase with sintered density, and modulus differences for the different W powders in Table II may be

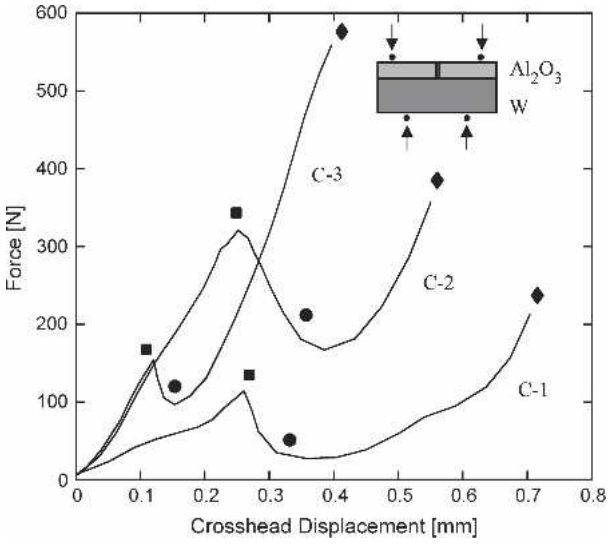

Fig. 3—Typical force-displacement curves obtained from the four-point bending delamination test. Representative test results for specimens from groups C-1, C-2, and C-3 are presented and the points at which interfacial crack initiation (■), crack propagation (●), and through-crack failure (◆) occurred are denoted. A schematic configuration of the delamination test is shown in the inset.

Table II. Flexural Modulus and Linear Shrinkage of Free-Standing, Single-Layer Specimens of W (from Powders of Series C) and Al_2O_3

Materials	Young's Modulus (GPa)	Linear Shrinkage (pct)
W (C-1)	23.2	0.8
W (C-2)	52.4	1.73
W (C-3)	54.5	2.85
Al_2O_3	0.2	0.1

attributed to the enhancement in sintering. The Al_2O_3 compact, on the other hand, sintered only weakly and had a very low degree of shrinkage (~0.1 pct) at our chosen sintering condition. The large average particle size (4 μm), low firing temperature, and high purity (*i.e.,* lack of sintering additives like SiO_2) all contributed to the low degree of sintering of Al_2O_3. As a consequence, the fired Al_2O_3 body was sound and could be handled without fragmenting, but the measured Young's modulus was extremely low.

For the co-sintered W/Al_2O_3 bilayer specimens, after the sintering cycle, most specimens were intact and no macroscopic interfacial cracks were present. The only exceptions to this observation were specimens from groups A-1 and A-5, which spontaneously delaminated during the firing cycle. For some groups of specimens, the W layer exhibited a relatively high degree of shrinkage as compared to the Al_2O_3 layer, leading to the development of slight curvature in the specimens, as can be seen in Figure 2(a).

Figure 3 illustrates some representative force-displacement curves obtained from the four-point bending delamination tests performed on the co-sintered W/Al_2O_3 specimens. Three typical stages can be identified over the duration of the test—initial elastic deflection, interfacial crack initiation and propagation, followed by elastic loading and through-crack failure of the W layer—as depicted by the symbols in the figure. The crack-propagation stage was manifested in these tests with both a load drop and a displacement excursion, owing to the use of displacement control. From one test to another, either symmetrical or asymmetrical interfacial cracking could be observed; in the latter case, the average of the crack-propagation forces for the left and right cracks is reported. In every case, the excursion in the load-displacement curve was correlated with direct observation of an interfacial crack. As an example, Figures 4(a) and (b), respectively, show a representative specimen before and after the critical crack-propagation stress was applied. In Figure 4(a) the geometry of the prenotch in the Al_2O_3 layer can be seen, whereas in Figure 4(b) the crack has deflected into the interface and debonded the joined layers. After the delamination stage, the final failure of the specimen occurred by the formation of a through-crack in the W layer, and in every case this failure occurred without any measurable plastic deformation. This is consistent with the relatively high ductile-to-brittle transition temperature of W[31] and the relatively low density (high defect content) of the partially sintered layer.

The test data in Figure 3 yield two critical loads of interest: the load at interfacial crack initiation (●), and that at through-crack failure of the W layer (◆). The first of these critical loads will be termed the *adhesive load*, P_a, and will be only briefly presented and discussed in this

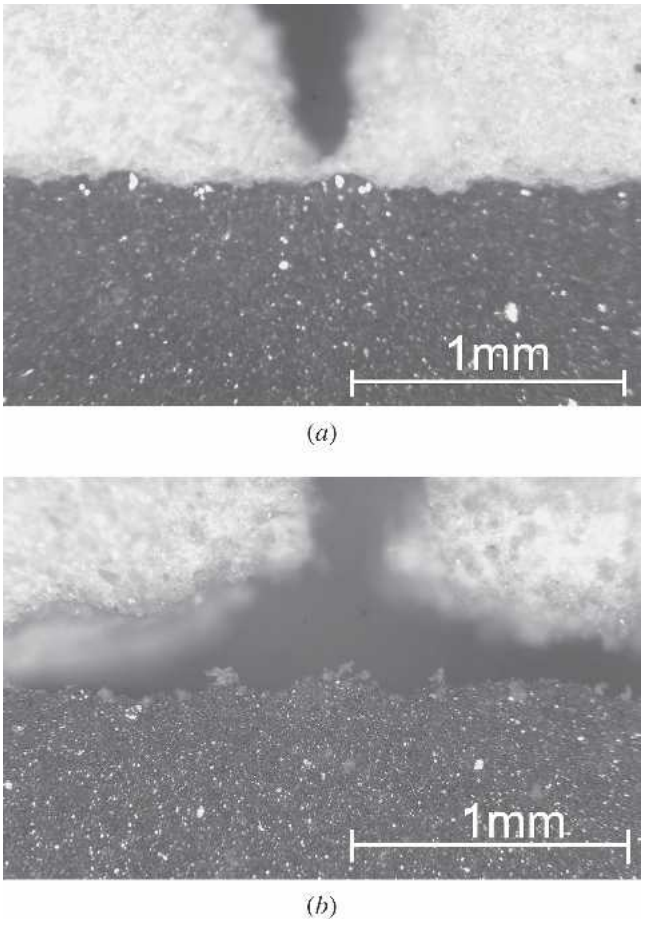

Fig. 4—Photographs of the notch region of a typical co-sintered W (bottom)/Al_2O_3 (top) specimen. In (*a*) the prenotch within the Al_2O_3 layer can be observed prior to the application of load, and in (*b*) interfacial delamination is seen after the critical load P_a has been applied.

section. The raw values of P_a are useful because they allow direct comparison of the apparent interfacial strength among the various specimens, whose geometry was identical. Later in this paper, the values of P_a will be used in a more quantitative analysis to determine the critical energy-release rate for interfacial fracture.

The second critical load, that corresponding to through-crack failure, is denoted P_f and can be used to determine the *fracture strength* of the W layer. This is because, after the arrest of interfacial cracks in the W/Al_2O_3 specimens, the W layer experiences a uniform bending moment between the two inner pins, with a maximum tensile stress, σ_f, across the top surface.[32] The tensile stress in this region is responsible for final rupture in the W layer, and because there was no significant plastic deformation before rupture, the fracture strength can be determined from:

$$\sigma_f = \frac{6P_f L}{bh_w^2} \qquad [2]$$

where L (=3.8 mm) is the horizontal distance between the inner and outer loading pins, b (=8.3 mm) is the width of the specimen, and h_W (=4.4 mm) is the thickness of the W layer.

The measured values of adhesive load and fracture strength for the various bilayer materials are plotted as a function of the monolayer coverage of sintering activators in Figures 5 and 6; each data point represents an average of three tests. Looking first at Figure 5, we see that the fracture strength of the W layer increased considerably with the concentration of sintering activators present in the system. This strengthening is a direct result of the enhancement of sintering and thus densification of W, as seen by prior researchers.[33] In contrast to the monotonic strength trend in Figure 5, the adhesion of the specimens, on the other hand, showed a more complex trend with activator concentration (Figure 6), first increasing, then peaking, and continuously decreasing. Note that in this plot, an adhesive load of zero indicates spontaneous delamination upon cooling after the firing cycle. Figure 6 also shows that the different series of specimens (*i.e.,* series A *vs* B or C) exhibited generally different degrees of adhesion. The different absolute adhesive loads measured between series A, B, and C could be due to many different factors, and we will return briefly to this issue at the end of this paper. The important point for the moment is that the same concave-downward trend with sintering activator concentration is observed in every case, and that improved sintering does not necessarily lead to improved adhesion if the activator content is too high (*i.e.,* beyond the peak in Figure 6). It is our purpose in what follows to understand the form of the trends in Figure 6, in terms of the various contributions to adhesion.

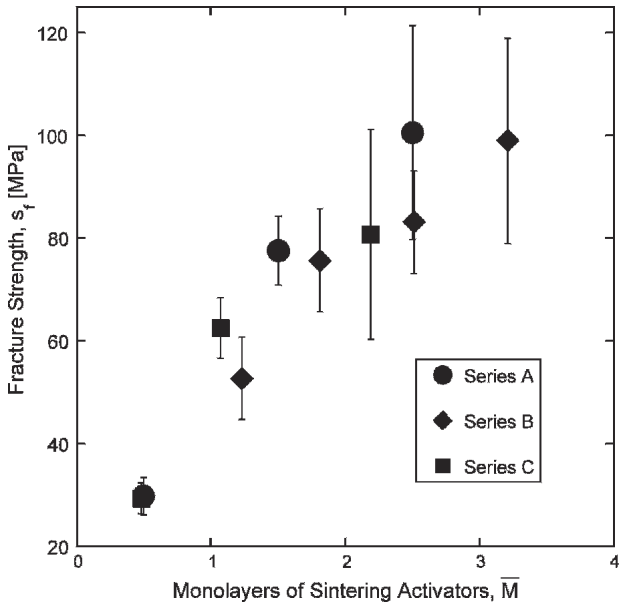

Fig. 5—Fracture strength σ_f of the W layer for various specimens as a function of the monolayer coverage of sintering activators. The plotted values are averages of three specimens, and the error bars denote the range of the three measurements.

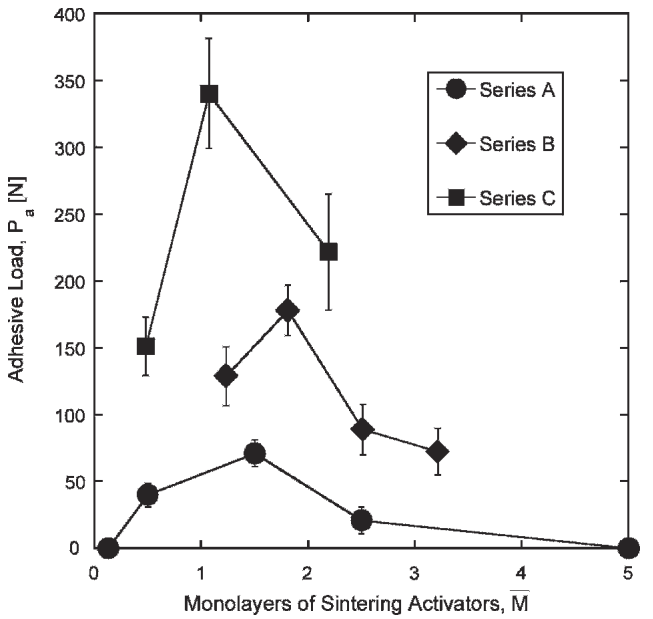

Fig. 6—Adhesive load P_a of the W/Al_2O_3 co-sintered compacts as a function of the monolayer coverage of sintering activators. As in Figure 5, the points represent an average of three tests and the error bars denote the range of measured values.

III. NUMERICAL ANALYSIS

The adhesive loads measured in Figure 6 can be influenced by several factors, which include: (1) Interfacial toughness between W and Al_2O_3, (2) Elastic properties and the mismatch of these properties between the W and Al_2O_3 layer, and (3) Specimen geometry.

Each of these factors can be influenced by the degree of sintering in the W layer, and therefore by the sintering activator concentration used. It is unclear from the experimental results alone which of the factors above controlled the observed trends in adhesive load. To decouple these effects, numerical modeling will be used in this section to extract the intrinsic interfacial toughness (*i.e.,* the critical strain energy-release rate for interfacial fracture) of bilayer W/Al_2O_3 specimens. Three specimen groups—C-1, C-2, and C-3—were chosen for the numerical study, as these specimens showed the sharpest characteristic trend in Figure 6.

A. *Modeling*

The numerical analysis was performed on the commercial finite element package ABAQUS, assuming isotropic linear elasticity and plane-strain conditions. The specimen geometry was assessed by careful dimensional measurements of the experimental specimens following the firing, to account for sintering-mismatch–related shape distortions. This geometry was then explicitly meshed as shown in Figures 7(a), (b), and (c) for the three specimen groups C-1, C-2, and C-3 used in the analysis; due to symmetry, only half of each specimen was modeled. While these models assume simple continua with a planar interface, our experimental materials actually contained some porosity in the joined bodies and across the joined interface. Therefore, the interfacial toughness values assessed in this study should be regarded as ''apparent'' toughness values, whose value is certainly lower than the interfacial toughness of identical materials without porosity.

The finite element model employed plane-strain eight-noded reduced integration isoparametric elements

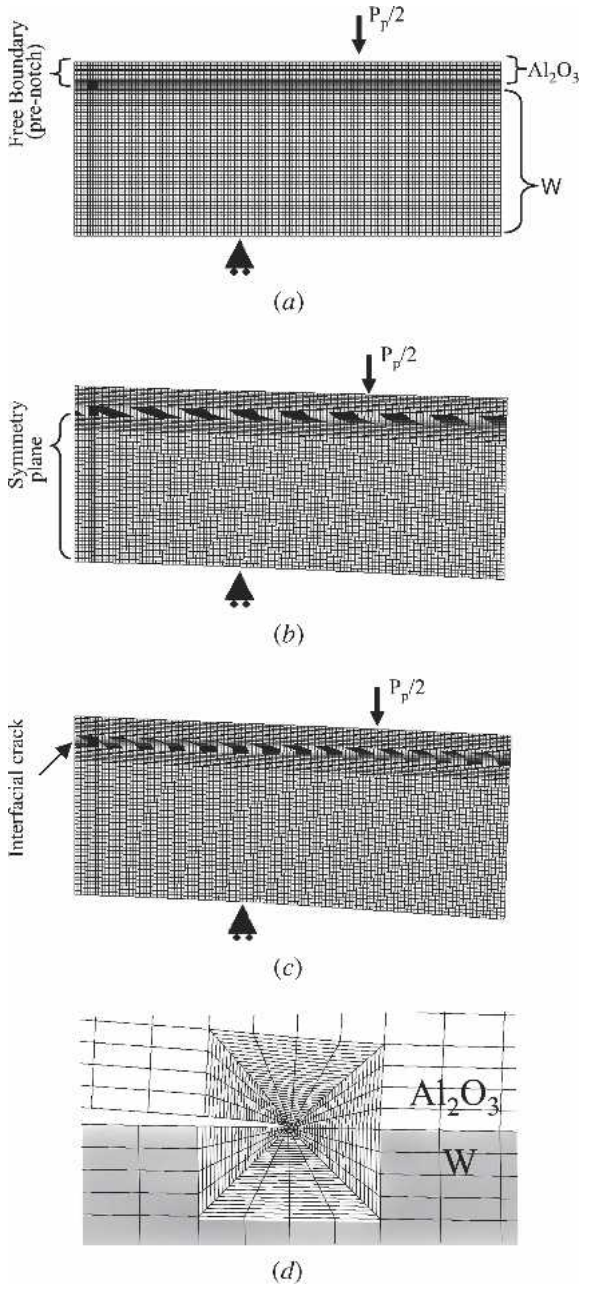

Fig. 7—The finite element models of specimens (*a*) C-1, (*b*) C-2, and (*c*) C-3, and (*d*) a zoomed view of a representative crack-tip region. Note the different degrees of shape distortion in the three specimens.

(CPE8R). A symmetry plane and a roller support were prescribed as boundary conditions (Figures 7(a), (b), and (c)). The interfacial cracks were assigned a length of 0.5 mm; a representative crack-tip region of the models is shown in Figure 7(d). Several inputs were used in the analysis, including Young's modulus, E, Poisson's ratio, ν, and the coefficients of thermal expansion (CTE) of the individual layers (Table III). The proper modulus values were obtained from the direct experimental measurements on monolithic W or Al_2O_3 materials (Table II), while the Poisson's ratio and CTE of W and Al_2O_3 were assumed to be the same as those of fully dense materials;[34–37] unlike modulus, these two properties are not significantly affected by porosity.[38,39] It should also be noted that the coefficient of thermal expansion of W is unaffected by minor Ni additions up to 0.4 wt pct.[34]

Two kinds of loads were prescribed in these models: thermal load and applied bending load. To simulate thermal stresses evolved during the cooling step following firing, a thermal excursion from 1177 °C to room temperature was applied to the simulated structures. The bending load was applied based on the experimental four-point bending delamination measurements by taking the load measured at crack propagation (P_p) for samples of series C, as given in Table III. For this purpose the load was measured just after the crack-initiation point in Figure 3, at a point when the interfacial crack was about 0.5 mm in length; this corresponds to the geometry of the finite element model in Figure 7.

For all of the numerical analyses, the thermal and bending loads were both applied in sequence to best simulate the true conditions of the experiments. To study the effect of geometric sintering distortion on the driving force for crack propagation, we also analyzed specimen C-3 with constant input parameters but with two different geometries: the highly distorted one shown in Figure 7(c) and a perfectly orthogonal specimen without distortion.

For all of the simulations described above, we determined the critical strain energy-release rate G_c and phase angle ψ for interfacial cracking. These are universal parameters that characterize interfacial toughness and were determined using a standard crack surface displacement method.[40,41] Specifically, the relative plane-strain displacements of two points on the top and bottom crack surfaces (Δu_x and Δu_y in the x and y directions, respectively) were determined, and subsequently used to derive the strain energy-release rate and phase angle according to Eqs. [3] and [4] below:

$$G_c = \frac{\pi(1+4\varepsilon^2)\cdot(\Delta u_x^2+\Delta u_y^2)}{8\lambda\cdot\left[\frac{(1-\nu_1)}{\mu_1}+\frac{(1-\nu_2)}{\mu_2}\right]} \quad [3]$$

$$\psi = \tan^{-1}\left(\frac{\Delta u_x}{\Delta u_y}\right) - \varepsilon\ln\left(\frac{\lambda}{h}\right) + \tan^{-1}(2\varepsilon) \quad [4]$$

In these equations, λ is the distance from the crack tip and h is the total thickness of the specimen. The parameter ε is known as the bimaterial constant and is given by:

$$\varepsilon = \frac{1}{2\pi}\ln\left[\frac{(3-4\nu_1)}{\mu_1}+\frac{1}{\mu_2}\right]\cdot\left[\frac{(3-4\nu_2)}{\mu_2}+\frac{1}{\mu_1}\right]^{-1}, \quad [5]$$

and μ is the shear modulus:

$$\mu_i = \frac{E_i}{2(1+\nu_i)} \quad [6]$$

In the above equations, the subscripts (i = 1 or 2) distinguish between Al_2O_3 (1) and W (2).

There is a closed-form analytical solution for the strain energy-release rate of a bilayer composite tested in the

Table III. Inputs and Outputs Used and Obtained in the Finite Element Analyses

Specimen	Input				Output	
	ν	CTE (ppm/K)	P_p (N)	P_a (N)	G_c (J/m^2)	ψ (deg)
W (C-1)	0.28	6.0				
W (C-2)	0.28	6.0				
W (C-3)	0.28	6.0				
Al_2O_3	0.22	8.3				
W/Al_2O_3 (C-1)			140	151	0.94	73.8
W/Al_2O_3 (C-2)			310	340	0.95	75.7
W/Al_2O_3 (C-3)			200	222	0.86	76.6

Poisson's ratio (ν) and CTE are from References 34–37, while bending load at crack propagation (P_p) was measured experimentally using the four-point bending delamination test in Figure 3. The outputs from the analyses include the critical strain energy–release rate (G_c) and the phase angle of the delamination failure (ψ).

four-point bending configuration, as derived by Charalambides *et al.*[25] That solution has been widely used to characterize interfacial toughness in various material systems[26,27,28] and extended to cover additional mechanical loads from thermal expansion stress.[42] However, the analytical solution is generally valid only when the interfacial crack size is relatively large ($a > 4\ h_{min}$, where h_{min} is the thinner of the two layer thicknesses) and a steady-state energy-release rate condition is established. With a shorter interfacial crack, such as we consider here ($a \sim h_{min}$), calculations based on the analytical solution could be in error by as much as 20 pct as compared with a complete numerical solution,[43] so we resort to the latter, more rigorous approach here.

B. *Simulation Results and Discussion*

Table III shows the critical strain energy-release rate and phase angle calculated from the finite-element analysis of bilayer composites C-1, C-2, and C-3 with the geometries in Figure 7. The phase angle in each case was $\psi = 75 \pm 2$ deg. The apparent interfacial toughness values for specimens C-1 and C-2 were comparable, 0.94 and 0.95 J/m^2 respectively, whereas that of specimen C-3 was somewhat lower at 0.86 J/m^2. The differences here do not seem to be associated with the different geometries induced by shrinkage mismatch; the values of G_c for specimen C-3 with and without the consideration of geometry distortion were determined to be 0.86 and 0.85 J/m^2, respectively. The different mechanical responses of specimen groups C-1 and C-2 *vs* C-3 must therefore lie in either the intrinsic interfacial toughness or the elastic properties of the sintered phases.

We begin our discussion of the results presented in Table III by first looking at specimen groups C-1 and C-2. Referring to Figure 6, we see that specimens from group C-2 exhibited a much higher adhesive load than did those from group C-1, and from the outputs presented in Table III it is clear that this occurred without a change in interfacial toughness. This suggests that the increased content of sintering activators and the attendant changes in sintering shrinkage did not appreciably affect the degree of mechanical interlocking at the interface in these materials. Instead, the increase of the adhesive load in specimen C-2 may be attributed to the increased stiffness of the W layer due to its higher content of sintering activators (specimen C-2 is more than twice as stiff as C-1 according to Table II). In other words, higher load was required to delaminate specimen C-2 because of the improved densification and higher elastic modulus of its W layer, even though the degree of mechanical interlocking in specimens from groups C-1 and C-2 was comparable.

Turning our attention now to a comparison of specimen groups C-2 and C-3, we see a different trend. Although the adhesive load in Figure 6 is significantly lower for specimens from group C-3 than for those from group C-2, the Young's modulus in Table II is very similar for the two groups of specimens. In this case the weakening of specimens from group C-3 may be due to a partial loss of mechanical interlocking and the change in morphology and distribution of pores along the interface, as reflected in the reduced apparent interfacial toughness value given in Table III. This reduction in G_c is likely a result of shrinkage mismatch between W and Al_2O_3, which is exacerbated at relatively high contents of Ni and Fe activators. Even though the magnitude of residual stresses that arise from shrinkage mismatch is generally much smaller than that of thermal stresses and they may be relaxed completely during the isothermal firing period, increased shrinkage mismatch is known to lead to the formation of interfacial defects,[7,17] and breakage of some mechanical interlocks at the interface may therefore be expected.

Combining the above modeling results, we can now review the origin of the concave-downward trend seen in all of the data sets in Figure 6. The initial increase in adhesive load with sintering activators stems primarily from densification of the individual layers, and the improved stiffness that derives therefrom. The weakening of the system that follows at higher levels of activation results from a degradation in the interface quality, apparently due to shrinkage mismatch that compromises the adhesion between layers. The extreme example of this case is specimen A-5 in Figure 6, which could not be prepared as a monolithic specimen but instead delaminated during firing, presumably due to mismatch stresses evolved on cooling.

These results may have some relevance for practical situations involving co-sintered systems, where the stress/load required to cause interfacial failure is of more importance than the interfacial fracture toughness: the sintering schedule, the concentration of sintering additives, and particle size must all be carefully controlled to optimize both

densification of the layers (which stiffens the system and increases P_a) and the shrinkage mismatch between layers (which degrades the interfacial toughness and lowers P_a). For example, for the W/Al_2O_3 bilayer system under investigation, relatively high values of P_a were obtained when the concentration of sintering activators in W fell somewhere between one and two monolayers. Recalling that powders C-1, C-2, and C-3 are representative of normal powder character variability that can be expected in an industrial setting, it is clear that control of impurities and conscious incorporation of sintering activators are required to optimize the mechanical strength of co-sintered systems. Finally, we note that although each of the three curves in Figure 6 has a similar shape, the positions of these curves are significantly different. This result is a consequence of other contributors to the system strength: particle size and particle size distribution can also have a significant influence on P_a because these parameters affect densification and potentially the mechanical interlocking along the joining interface when powders of different sizes are used.

IV. CONCLUSIONS

Four-point bending delamination experiments were used to evaluate the strength and adhesion of co-sintered W/A_2O_3 bilayer composites. By varying the concentration of sintering activators in the W layer, the shrinkage mismatch and sintered properties of the composite were manipulated to evaluate their individual contributions to the adhesion of co-sintered materials. It was observed that the adhesion of the bilayer (as measured by the load applied at delamination) exhibited an unusual trend with increasing content of sintering additives, first increasing and then decreasing. Numerical finite element analyses suggest that the initial increase in adhesive strength can be attributed to the enhancement in sintering and hence improved stiffness of the W layer, whereas the decrease of adhesive load at relatively high additive contents is a result of interface weakening. The expected breakage of some mechanical interlocks at the interface due to a higher degree of shrinkage mismatch is consistent with this result. Consequently, to maximize the adhesive strength of a co-sintered bilayer, both the densification-related properties of the individual layers and the sintering mismatch should be carefully controlled through the use of sintering additives and other sintering protocols.

ACKNOWLEDGMENTS

The authors express their sincere gratitude to Professor T.W. Eagar and Professor D.M. Parks (MIT) for valuable discussions and support.

REFERENCES

1. R.F. Bunshah: *J. Vac. Sci. Technol. B*, 1984, vol. 2, pp. 789-99.
2. M.J. Pomeroy: *Mater. Des.*, 2005, vol. 26, pp. 223-31.
3. L.G. Vettraino and S.H. Risbud: *IEEE Trans. Compon. Packag. Technol.*, 1999, vol. 22, pp. 270-81.
4. A.J. Blodgett: *Sci. Am.*, 1983, vol. 249, pp. 86-96.
5. D.L. Wilcox, F.H. Rong, and D. Anderson: *Proc. Int. Symp. Microelectron.*, 1997, vol. 3235, pp. 17-23.
6. L.A. Xue, T.L. Cable, and E.A. Barringer: *Ceram. Eng. Sci. Proc.*, 2003, vol. 24, pp. 281-86.
7. T. Cheng and R. Raj: *J. Am. Ceram. Soc.*, 1989, vol. 72, pp. 1649-55.
8. K. Otsuka, T. Usami, and M. Sekihata: *Am. Ceram. Soc. Bull.*, 1981, vol. 60, pp. 540-45.
9. K. Biswas and G.S. Upadhyaya: *Mater. Des.*, 1998, vol. 19, pp. 231-40.
10. J.R. Floyd: *Am. Ceram. Soc. Bull.*, 1963, vol. 42, pp. 65-70.
11. B.C. Foster, F.J. Bachner, E.S. Tormey, M.A. Occhionero, and P.A. White: *IEEE Trans. Components Hybrids Manuf. Technol.*, 1991, vol. 14, pp. 784-89.
12. D.A. Chance: *Metall. Trans.*, 1970, vol. 1, pp. 685-94.
13. S.J. Howard, R.A. Stewart, and W.J. Clegg: *Key Eng. Mater.*, 1996, vol. 116–117, pp. 331-50.
14. T.W. Clyne and S.C. Gill: *J. Therm. Spray Technol.*, 1996, vol. 5, pp. 401-18.
15. H. Tomaszewski, J. Strzeszewski, and W. Gebicki: *J. Eur. Ceram. Soc.*, 1999, vol. 19, pp. 255-62.
16. X. Wang and P. Xiao: *Acta Mater.*, 2004, vol. 52, pp. 2591-603.
17. P.Z. Cai, D.J. Green, and G.L. Messing: *J. Am. Ceram. Soc.*, 1997, vol. 80, pp. 1929-39.
18. R.R. Tummala: *Am. Ceram. Soc. Bull.*, 1988, vol. 67, pp. 752-58.
19. W.H. Kohl: *Vacuum*, 1964, vol. 14, pp. 333-54.
20. P.F. Varadi and R. Dominguez: *Am. Ceram. Soc. Bull.*, 1966, vol. 45, pp. 789-91.
21. P.S. Kislyi, B.D. Storozh, and M.L. Gorb: *Sov. Powder Metall. Met. Ceram.*, 1977, vol. 16, pp. 299-302.
22. R.M. German and Z.A. Munir: *Metall. Trans. A*, 1976, vol. 7A, pp. 1873-77.
23. N.M. Hwang, Y.J. Park, D.Y. Kim, and D.Y. Yoon: *Scripta Mater.*, 2000, vol. 42, pp. 421-25.
24. I.H. Moon, J.Y. Kim, and Y.D. Kim: *Int. J. Refract. Met. Hard Mater.*, 1984, vol. 3, pp. 176-79.
25. P.G. Charalambides, J. Lund, A.G. Evans, and R.M. McMeeking: *J. Appl. Mech.*, 1989, vol. 56, pp. 77-82.
26. A. Cazzato and K.T. Faber: *J. Am. Ceram. Soc.*, 1997, vol. 80, pp. 181-88.
27. P. Lucksanasombool, W.A.J. Higgs, R.J.E.D. Higgs, and M.V. Swain: *Biomaterials*, 2003, vol. 24, pp. 1159-66.
28. J. Malzbender, R.W. Steinbrech, and L. Singheiser: *J. Mater. Res.*, 2003, vol. 18, pp. 929-34.
29. A.J. Phillipps, W.J. Clegg, and T.W. Clyne: *Acta Metall. Mater.*, 1993, vol. 41, pp. 819-27.
30. Z. Suo and J.W. Hutchinson: *Mater. Sci. Eng.*, 1989, vol. A107, pp. 135-43.
31. L.L. Seigle and C.D. Dickinson: *Refractory Metals and Alloys*. 1963, Interscience Publishers, New York, NY, vol. 17, pp. 65-117.
32. S.H. Crandall, N.C. Dahl, and T.J. Lardner: *An introduction to the Mechanics of Solids*. 1999, McGraw-Hill: New York, NY, pp. 416-510.
33. C.J. Li and R.M. German: *Metall. Trans. A*, 1983, vol. 14A, pp. 2031-41.
34. Y.H. Kim, S.H. Cho, J.K. Lee, and I.H. Moon: *Int. J. Refract. Met. Hard Mater.*, 1988, vol. 7, pp. 206-09.
35. J.F. Shackelford and W. Alexander: *CRC Materials Science and Engineering Handbook,* 3rd ed. 2001, CRC Press, Boca Raton, FL, p. 462.
36. W.B. Eisen: *ASM Handbook: Powder Metal Technologies and Applications*. 1998, ASM, Materials Park, OH, p. 907.
37. G.T. Murray: *Handbook of Materials Selection for Engineering Applications*. 1997, Marcel Dekker, Inc., New York, NY, p. 263.
38. D.N. Boccaccini and A.R. Boccaccini: *J. Nondestr. Eval.*, 1997, vol. 16, pp. 187-92.
39. L.J. Gibson and M.F. Ashby: *Cellular Solids: Structure & Properties*. 1988, Pergamon Press: Elmsford, NY, p. 207.
40. J.R. Rice: *J. Appl. Mech.*, 1988, vol. 55, pp. 98-103.
41. P.P.L. Matos, R.M. McMeeking, P.G. Charalambides, and M.D. Drory: *Int. J. Fract.*, 1989, vol. 40, pp. 235-54.
42. P.G. Charalambides, H.C. Cao, J. Lund, and A.G. Evans: *Mech. Mater.*, 1990, vol. 8, pp. 269-83.
43. S. Roham, K. Hardikar, and P. Woytowitz: *J. Mater. Res.*, 2004, vol. 19, pp. 3019-27.